Ultra-low-density digitally architected carbon with a strutted tube-in-tube structure

Ye, Jianchao; Liu, Ling; Oakdale, James; Lefebvre, Joseph; Bhowmick, Sanjit; Voisin, Thomas; Roehling, John D; Smith, William L; Cerón, Maira R; van Ham, Jip

Published in:
Nature Materials

DOI:
10.1038/s41563-021-01125-w

Publication date:
2021

ARTICLES
https://doi.org/10.1038/s41563-021-01125-w

nature materials

Check for updates

Ultra-low-density digitally architected carbon with a strutted tube-in-tube structure

Jianchao Ye[1,6]✉, Ling Liu[2,6], James Oakdale[1], Joseph Lefebvre[3], Sanjit Bhowmick[3], Thomas Voisin[1], John D. Roehling[1], William L. Smith[4], Maira R. Cerón[1], Jip van Ham[2], Leonardus Bimo Bayu Aji[1], Monika M. Biener[1], Y. Morris Wang[1,5], Patrick R. Onck[2]✉ and Juergen Biener[1]✉

Porous materials with engineered stretching-dominated lattice designs, which offer attractive mechanical properties with ultra-light weight and large surface area for wide-ranging applications, have recently achieved near-ideal linear scaling between stiffness and density. Here, rather than optimizing the microlattice topology, we explore a different approach to strengthen low-density structural materials by designing tube-in-tube beam structures. We develop a process to transform fully dense, three-dimensional printed polymeric beams into graphitic carbon hollow tube-in-tube sandwich morphologies, where, similar to grass stems, the inner and outer tubes are connected through a network of struts. Compression tests and computational modelling show that this change in beam morphology dramatically slows down the decrease in stiffness with decreasing density. In situ pillar compression experiments further demonstrate large deformation recovery after 30–50% compression and high specific damping merit index. Our strutted tube-in-tube design opens up the space and realizes highly desirable high modulus–low density and high modulus–high damping material structures.

Monolithic porous ultra-low-density materials have many emerging applications, such as mechanical shock absorbers, thermal and acoustic insulation, flexible battery and catalyst scaffolds, micro-electromechanical devices and high-energy-density physics[1–6]. Some of these applications, for example, carbon scaffolds for battery electrodes, will benefit from reducing the inactive carbon material density while still providing high specific surface area combined with high stiffness and shape-recovery properties[7,8]. The main challenge in further developing ultra-low-density structural materials is to overcome the rapid deterioration of the mechanical properties with decreasing density. In the first generation of low-density carbon materials (that is, carbon aerogels), the stiffness decreased very rapidly with decreasing density due to their stochastic or poorly connected structures[9–11]. By improving the network connectivity, the decrease in stiffness was considerably reduced in carbon nanotube networks and graphene foams[8,12–17]. However, despite the exceptionally high intrinsic stiffness of the individual structural units (that is, the Young's modulus (E) of carbon nanotubes or single-layer graphene is ~1 TPa), three-dimensional (3D) assemblies still exhibit much lower moduli at low density than is predicted theoretically. More recently, additive manufacturing techniques have enabled considerably more complex architectures with precisely defined geometries and deformation modes[1,6,18–22]. For example, 3D graphene prepared via direct ink writing (DIW)[19,20] shows improved specific moduli compared with bulk monoliths of identical density, which has been attributed to the controlled and ordered macroscale structure of the printed materials[20]. Advances in direct laser writing-two photon polymerization (DLW-TPP) now enable the exploration of computer-designed architectures[23–25], as well as nanoscale size effects on the material properties[2], which, for example, allow the realization of six times greater strength in a DLW-TPP-derived carbon nanolattice with beams three orders of magnitude smaller than vitreous carbon microlattices[26]. In most studies on architected pyrolytic carbons[2,24,25,27], samples were prepared by direct pyrolysis of printed structures, leading to large linear shrinkage (up to 80%) and relatively high densities (>100 mg cm^{-3}). Although the modulus and strength of these carbon materials are close to the theoretical limit at high densities, the scaling exponent of these lattice designs can still be higher than 1 when reducing the density[2,25]. This has been attributed to the presence of fabrication defects, frozen joints and the finite size of the structure[2,25]. It is therefore believed that, besides the use of stretching-dominated lattice designs (such as the octet-truss), careful design of the beam itself may be of critical importance for maintaining high stiffness at low densities. In response to this need, hollow-tube beam designs have been developed to improve the stiffness of microlattices at low densities[1]. Still, the scaling exponent for octet-truss hollow-tube Al_2O_3 remains larger than expected (1.6 versus 1) due to compliant shell-wall bending of thinner tubes triggered by stress concentration at the nodes. Computer-aided fractal-like hierarchical beam designs[28,29] have shown great potential in further stiffening the low-density structure and achieving near-constant specific strength, by precisely tuning the deformation modes at different length scales, although the smallest achievable tube size is currently limited by the resolution of the additive manufacturing techniques (~ 1 μm).

In this work, we address this problem by developing a stiffer hollow-tube design based on a strutted tube-in-tube (STinT) sandwich morphology. Specifically, we demonstrate the concept by fabricating carbon-based microlattices with integrated

[1]Materials Science Division, Physics and Life Sciences Directorate, Lawrence Livermore National Laboratory, Livermore, CA, USA. [2]Micromechanics of Materials, Zernike Institute for Advanced Materials, University of Groningen, Groningen, Netherlands. [3]Bruker, Minneapolis, MN, USA. [4]Materials Engineering Division, Engineering Directorate, Lawrence Livermore National Laboratory, Livermore, CA, USA. [5]Department of Materials Science and Engineering, University of California, Los Angeles, CA, USA. [6]These authors contributed equally: Jianchao Ye, Ling Liu. ✉e-mail: ye3@llnl.gov; p.r.onck@rug.nl; biener2@llnl.gov

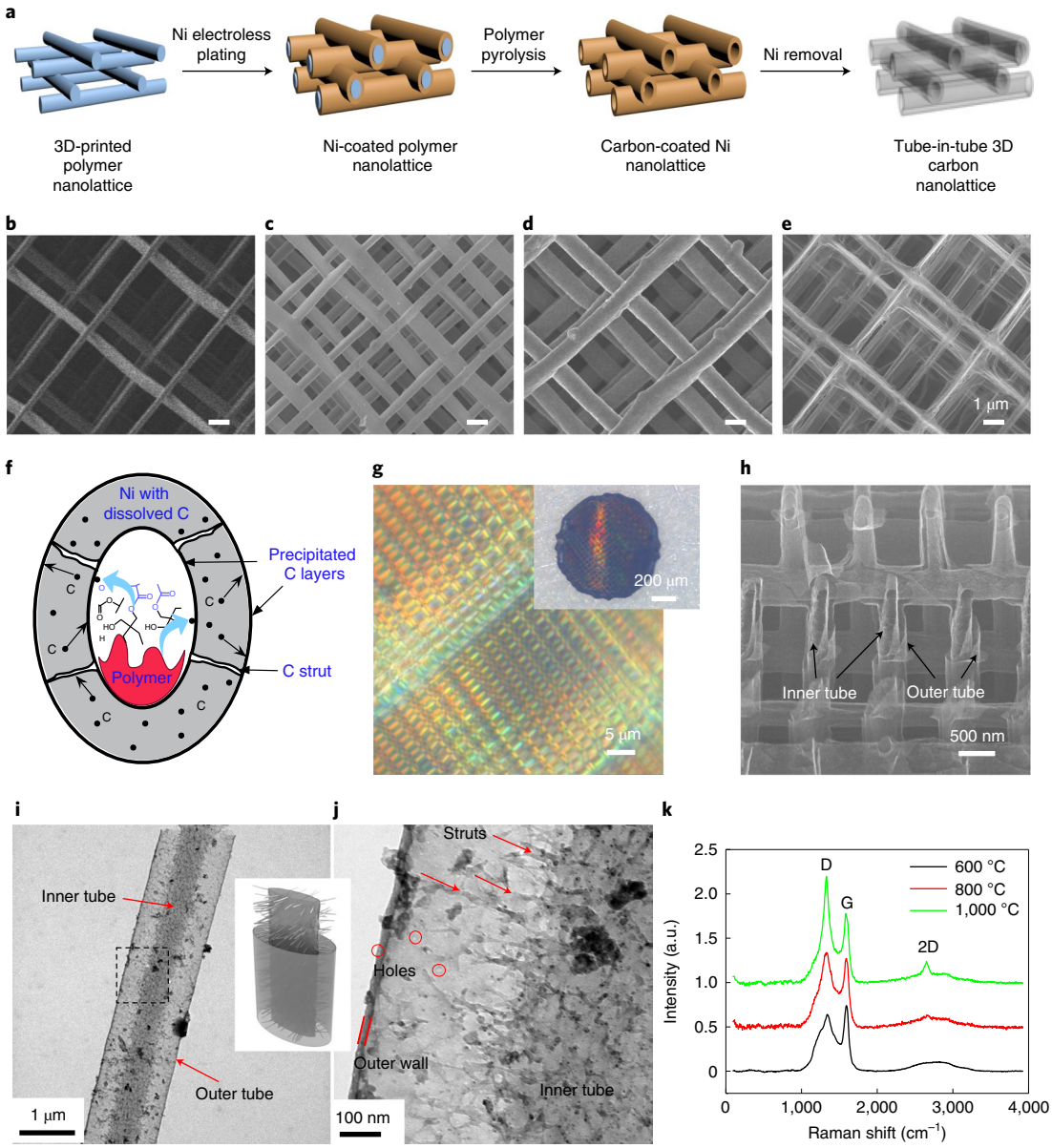

Fig. 1 | 3D printing and post processing to convert solid polymeric beams into STinT carbon structures. a, Illustration of the two-step templating approach developed to convert 3D-printed polymer microlattices into STinT carbon. **b**–**e**, SEM images of corresponding structures after each process: 3D-printed polymer nanolattice (**b**); Ni-coated polymer nanolattice (**c**); carbon-coated Ni nanolattice (**d**); tube-in-tube 3D carbon nanolattice (**e**). Scale bars, 1 μm. **f**, Illustration of the Ni-catalysed polymer pyrolysis. **g**, Optical images of an STinT carbon plate with 3 μm pitch size. The colour is a result of optical interference on the periodic pattern. **h**, SEM image of a fractured STinT carbon sample with exposed inner tubes. **i**, A bright-field TEM image of a STinT carbon beam. Inset is a 3D illustration of STinT carbon morphology. **j**, Zoomed-in image from **i** showing the preferentially radially aligned nano-struts (arrows). **k**, Raman spectra of STinT carbons obtained under 600, 800 and 1,000 °C pyrolysis temperatures.

STinT beam morphology through a two-step nickel-catalysed templating-pyrolysis process (Fig. 1a). This fabrication process maintains the structure and dimensions of the as-printed sacrificial polymer template to deliver remarkably stiff carbon lattices with densities as low as 6.4 mg cm^{-3}. We attribute the stiffness of our low-density carbon lattices to the integrated nanoscale strutted tube-in-tube beam design, which enables lightweight but stiff lattice building blocks. Our design concept can be applied orthogonal to current lattice topology optimization developments, opening up a synergetic, still unexplored path towards low-density high-stiffness carbon-based lattice materials. Using our STinT technology, we demonstrate the fabrication of pyrolytic carbon structures in the high stiffness–ultra-low-density region of the stiffness–density property map. Finite element analyses revealed that the consistently high stiffness at decreasing densities is a consequence of the coupling of the STinT tube spacing with the density of the lattice structure, which leads to strengthening of the tube joints and an increase of the flexural modulus of the tubes via an enlarged outer tube diameter and preferable mass distribution at lower densities. While this intrinsic coupling prevents the derivation of a self-similar scaling relationship, such highly efficient mechanical behaviour has rarely been reported.

The fabrication of these low-density STinT carbon materials starts with printing of a highly cross-linked acrylic polymer template (Fig. 1b) via DLW-TPP[30]. The polymer template is first coated with a stiff conformal Ni layer through electroless plating (Fig. 1c)[29]

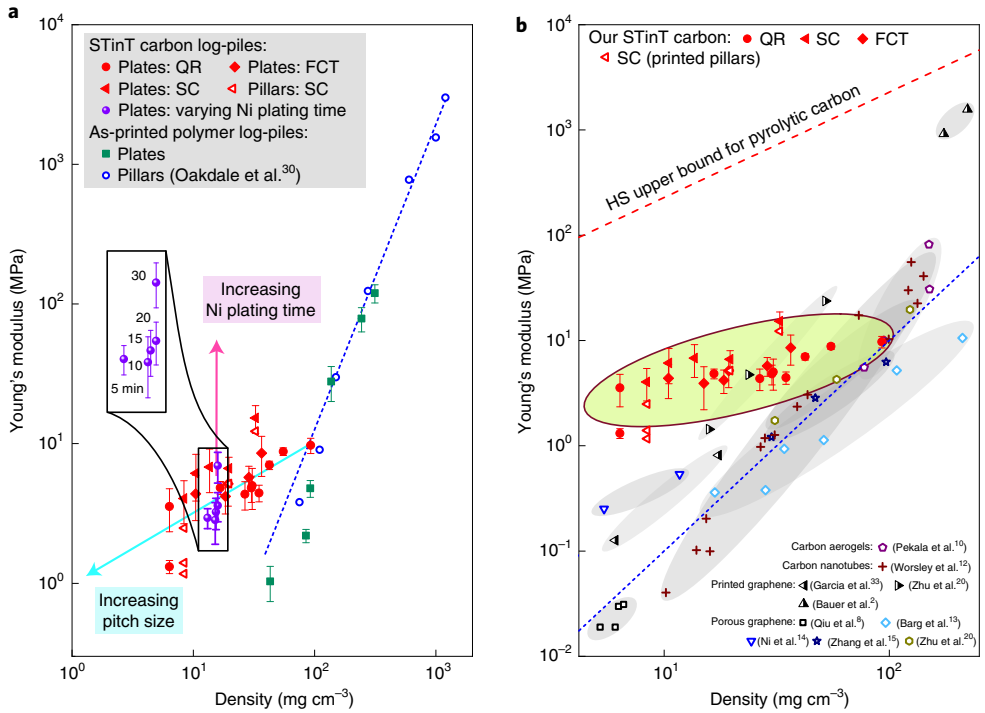

Fig. 2 | Young's modulus of the STinT carbon structures and comparison with other materials. a, A comparison of Young's modulus versus density between the as-printed polymer template and the converted carbon structure. The polymer data were taken from a collection of samples with varying *x*–*y* spacing but with the same beam diameter. The carbon data were taken from a collection of samples with varying *x*–*y* spacing, beam diameter and coating time. The purple spheres in the inset show the effect of increasing Ni plating time in plate samples, corresponding to the structural and mechanical data shown in Supplementary Table 4 and Fig. 3a. The blue dashed line represents a scaling exponent of 2. The turquoise arrow line is a guide to the eye. **b**, A summary of Young's modulus as a function of density compared with 3D porous carbon materials reported in the literature. The symbols in red are from our STinT carbon samples. The blue dashed line represents a scaling exponent of 2. Literature data can be found in refs. [2,5,8,10,12–15,19,20,30]. HS, Hashin–Shtrikman. Error bars were determined by testing at least three different positions on the plate samples.

and then pyrolyzed to convert the polymeric carbon into a graphitic double tubular carbon structure using the catalysing effect of the Ni layer (Fig. 1d). Removing the Ni coating by a wet etching process then releases the unique tube-in-tube morphology characteristic of our STinT carbon materials (Fig. 1e,g–j). Details of the STinT carbon fabrication process are provided in Methods. We note that the fabrication of 3D porous graphene structures using a Ni-catalysed synthesis approach has been reported previously[31–33]. The fabrication process described in this work results in a distinctive tube-in-tube morphology with unique mechanical behaviour, as reflected by a persistently high modulus at low densities.

The 3D morphology and overall sample shape of the polymer microlattice template are maintained during pyrolysis and Ni etching. For a pyrolysis temperature of 600 °C, no macroscale shrinkage or warpage was observed (Fig. 1g for top view and Supplementary Fig. 1 for a cross-sectional view). Microscale tube waviness may exist, possibly due to surface roughness of the electroless-plated Ni layer and capillary force-induced collapse in the subsequent etching/drying steps. The initial solid polymer beams of the structure are converted into a nanometre-thick double tubular carbon structure, as is clearly revealed by scanning electron microscopy (SEM) images from an intentionally broken sample (Fig. 1h). The exact morphology of the STinT carbon is controlled by the sacrificial polymer template and the thickness of the Ni catalyst layer. Transmission electron microscopy (TEM) (Fig. 1i,j) and TEM tomography (Supplementary Information and Supplementary Videos 1–3) provide further details of the intricate structure of STinT carbon. In contrast to the smooth appearance of the outer tube, the inner tube has a rougher morphology, making it more difficult to determine the exact thickness of the inner tube wall. Radially grown nano-struts with diameter <10 nm connect the inner tube with the outer tube (Fig. 1j). Similar sandwich panel designs with integrated load-bearing struts are also found in nature, where lightweight and good mechanical properties are important. Examples include the skulls of various species[34,35], stems of plants[36,37] and bird bones in general[38,39]. While our STinT carbon structure resembles the architecture of animal skulls and plant stems, its characteristic length scale is orders of magnitude smaller. The empty space inside the inner tube of bird bones is also filled with struts, a design feature that is not present in our current approach but which could potentially be integrated through photoresist design, for example, by adding carbon nanotubes[40] or by using resin formulations that generate porous polymer print lines[41]. This increases the number of design parameters that can be used for further optimization of the STinT structure.

Selected area electron diffraction patterns from the inner and outer tube areas (Supplementary Information and Supplementary Fig. 2) both show broad graphitic rings indicating limited long-range order. The poor crystallinity revealed by selected area electron diffraction is consistent with the observation of a strong D band and a weak 2D band in Raman analysis (Fig. 1k) and is a consequence of the relatively low pyrolysis temperature (600 °C). The low pyrolysis temperature also results in relatively high residual oxygen and hydrogen contents of ~11.6 and 14.9 at% on the basis of energy-dispersive spectroscopy (EDS) (Supplementary Table 1) and elastic recoil detection analysis (ERDA, Supplementary Fig. 3).

The mechanical behaviour of STinT carbons was characterized using both flat-punch and micropillar compression tests. For

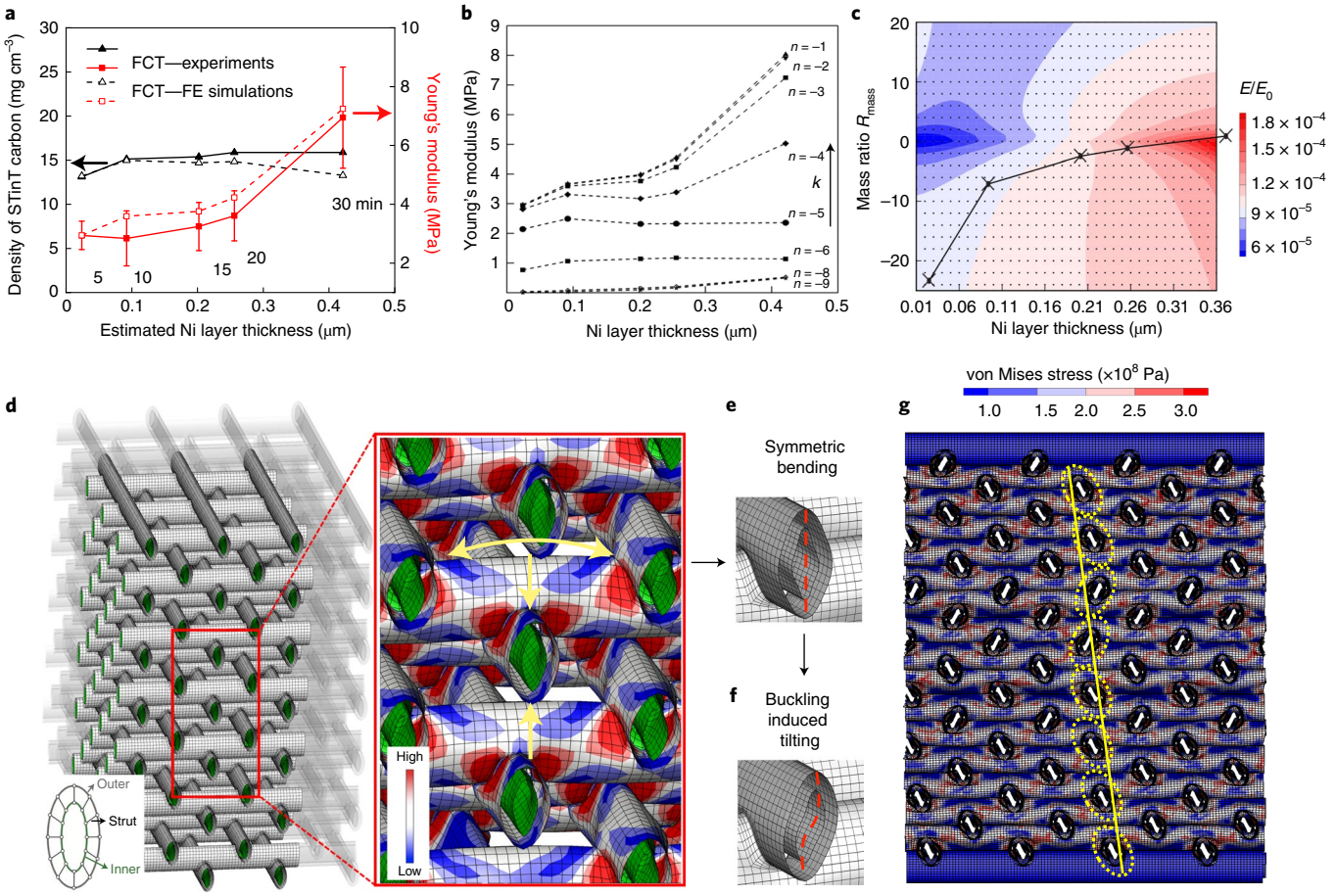

Fig. 3 | Finite element modelling. a, Comparison of Young's moduli obtained from FE simulations and experiments, plotted together with the experimentally measured sample densities and the density values of the corresponding FE models (calculated from the tube diameter and thickness values provided in Supplementary Table 4 and assuming a density of 1.4 g cm^{-3} for the graphitic walls of the STinT structure). The Ni-layer thickness is controlled by the plating time (indicated). **b**, The effect of the nano-strut stiffness k on the overall Young's modulus of the STinT carbon structure. The strut stiffness accounts for the effective connectivity between the outer and inner tubes, which varies from strongly connected (for example, high k) to fully detached (for example, extremely low k). The stiffness is defined as $k = 10^n \times E_0$ μm, with n varying between −1 and −9. **c**, Effect of mass ratio, defined by $R_{mass} = (M_{outer} - M_{inner})/\min(M_{outer}, M_{inner})$, and the spacing between the inner and outer tube spacing (controlled through the Ni-layer thickness) on the relative Young's modulus as predicted by FE modelling. In general, the modulus increases from left to right with increasing Ni-layer thickness. Experimental values from **a** are superimposed (crosses). M_{outer} and M_{inner} are the masses of the outer and inner tubes, respectively. **d**, FE model or the FCT STinT carbon structure (left) and a detailed contour plot for the von Mises stress superimposed on the outer carbon surface (right), revealing two deformation mechanisms at low strains: local symmetric bending (vertical arrow) and longitudinal bending (curved horizontal arrow). The staggering pattern is FCT and the pitch size is 5 μm. **e**, The symmetric bending of a tube-in-tube unit right before column buckling (strain slightly smaller than 0.056). **f**, Tilted buckling of the tube-in-tube unit right after column buckling, which corresponds to the sudden drop of load shown in Supplementary Fig. 11b. **g**, Synergistic tube-in-tube buckling that ensues with column buckling.

as-printed polymeric samples, the flat-punch indentation moduli from disk samples (Fig. 2a) are overlapping with previously reported moduli from micropillar compression tests[30], which indicates that flat-punch indentation is as effective as pillar compression in extracting the mechanical properties[42]. The modulus–density scaling relationship, $E \propto \rho^n$ shows an exponent n of ~2, consistent with the bending-dominated deformation mode[43] of log-pile structures and previously reported data[44]. However, the mechanical performance deteriorates faster when the density is less than 100 mg cm^{-3}, which is probably due to manufacturing defects.

Interestingly, the moduli of the STinT carbon log-pile structures decrease much more slowly with decreasing density compared to their polymeric counterparts. Specifically, moduli derived from STinT plate samples decrease only by a factor of ~4, from 10 MPa to 2.5 MPa, while the density decreases by a factor of 16, from 100 mg cm^{-3} to 6.4 mg cm^{-3}, showing that the material is maintaining its high stiffness with decreasing density.

The tube-in-tube structure makes STinT carbon log-pile structures over ten times stiffer than other carbon nanomaterials[8,12,14,19] in the ultra-low-density regime (≤10 mg cm^{-3}) (Fig. 2b). A summary of the STinT carbon geometries and corresponding mechanical properties can be found in Supplementary Table 2. As discussed later, the STinT structure becomes more advantageous with decreasing density as the diameter of the outer tube of STinT carbon is inversely coupled to the density of the polymeric template; as the pitch of the polymeric template increases with decreasing density, the thickness of the Ni coating increases for a given plating time. With a density of 6.4 mg cm^{-3}, the quasi-random (QR, random stacking with fixed vertical stack spacing) STinT carbon demonstrates a modulus of 1–4 MPa, which is about ten times higher than freeze-casted

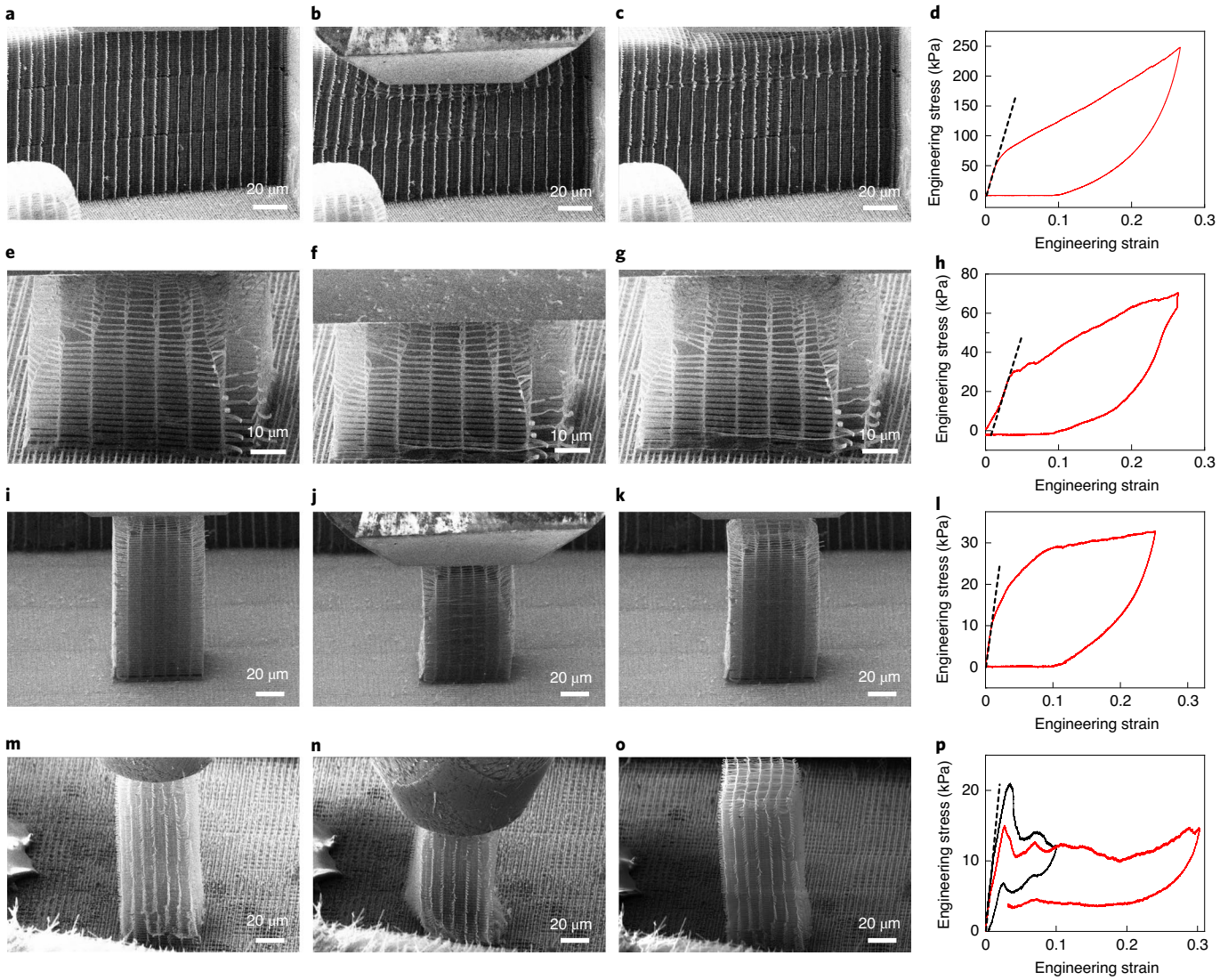

Fig. 4 | In situ SEM compression tests with varying sample aspect ratios and architectures. a–p, A bulk sample (5 μm pitch, 15.1 mg cm^{-3}) (**a–d**) and simple cubic log-pile STinT carbon pillars (10 μm pitch, 8.4 mg cm^{-3}) with various height/width aspect ratios ranging from 1:1 (**e–h**) to 2:1 (**i–l**) and 2.5:1 (**m–p**); 25° SEM images before loading (**a**,**e**,**i**,**m**), at 30% strain (**b**,**f**,**j**,**n**) and after release (**c**,**g**,**k**,**o**). Corresponding engineering stress–strain curves (**d**,**h**,**l**,**p**) with **p** showing two consecutive engineering stress–strain curves, first to 10% strain (black) and then to 30% strain (red). Engineering stress–strain curves were corrected by subtracting base plane deformation. Young's moduli of the four samples from top to bottom are 4.56 MPa, 1.17 MPa, 1.43 MPa and 2.49 MPa, respectively.

cellular graphene with a laminar structure[14] and DIW reduced graphene oxide structures[19] that are made from random porous building blocks[14,19]. For simple cubic (SC) STinT log-pile structures, the stiffness is even higher. Compared with previously reported micro- and nano-architected (octet-truss, gyroid, cubic, nanospinodals) pyrolyzed carbon materials with solid beams and typical densities of >100 mg cm^{-3} (refs. [23–25,27], our STinT carbons have lower densities (<100 mg cm^{-3}) but show superior moduli compared to other carbonaceous materials at similar densities and strongly outperform these in the low-density regime (Fig. 2b). The Young's modulus of the lowest density STinT carbon log-piles (≤10 mg cm^{-3}) is also higher than that of NiP microlattices and close to Al_2O_3 single-tube octet-trusses (Supplementary Fig. 4)[1,18,45]. However, compared with the theoretical Hashin–Shtrikman upper bound[46], there still remains a two orders of magnitude gap to be filled in future studies.

Our data in Fig. 2 roughly follow a modulus–density relationship that can be captured by a power law, with an exponent of approximately 0.5, which is much lower than that of all other previously reported porous materials (Supplementary Table 3). We note, however, that theoretical scaling laws require that the underlying topologies of all considered data points are mechanically similar. The smallest and best physically possible scaling exponent is defined by the Hashin–Shtrikman upper bound, which equals 1 (indicating stretching-dominated behaviour). The observation of a modulus–density relationship that follows a power law with an exponent of approximately 0.5 in our work thus immediately reveals that the above-mentioned condition of topological equivalence is not met. Indeed, with the decrease of density, not only does the log-pile pitch size increase, but so does the outer tube diameter. It is common in many reported low-density porous materials that a change of density is achieved by simultaneously changing more than one independent geometrical parameter (Supplementary Table 3). As discussed later in more detail, a distinct difference of the STinT carbon process compared with other processing techniques is that reducing the density leads to a microstructure that is more efficient in transmitting the applied load.

The beneficial effects of the STinT structure are captured by a straightforward calculation (Supplementary Fig. 5) that compares a double tube structure with a single tube structure. It also correctly predicts that a thicker Ni layer (larger outer tube diameter) and a redistribution of carbon mass towards the outer tube will lead to a higher moment of inertia and, therefore, a higher flexural modulus. This prediction is consistent with mechanical tests of STinT carbons with the same density and pitch (for more details see the discussion below), where increasing the Ni-coating thickness from 0.05 to 0.45 µm increases the modulus from 3 MPa to 7 MPa (Figs. 2a and 3a).

Finite element (FE) simulations were performed to further illuminate the origin of the high stiffness at low density (for details on the numerical implementation see Methods and the Supplementary Information). The simulation framework of the face-centred tetragonal (FCT) STinT carbon structure is depicted in Fig. 3d (for the SC and QR structures, see Supplementary Fig. 6). All modelled STinT structures feature stiff nano-struts between the inner and outer carbon tubes (see schematic inset in Fig. 3d). According to the FE results, the primary deformation mode at low strain values is local symmetric bending at the elliptical tube surfaces near the scaffold joints (see the von Mises stress contours in Fig. 3d and the symmetric local bending mode in Fig. 3e) when the horizontally aligned tubes are compressed and indented by the adjacent orthogonal tubes. The secondary mode is the longitudinal bending of tubes, illustrated by the exaggerated deformation in Fig. 3d.

The key feature that explains the small reduction in stiffness with decreasing density is the increase in nickel-coating thickness with increasing log-pile spacing, supplemented by carbon mass redistribution from the inner to the outer tubes. To isolate these microstructural aspects, we performed control experiments for one template geometry (fixed density and pitch) in which we systematically varied the nickel plating time from 5 to 30 minutes, leading to the microstructural length scales in Supplementary Table 4. These data were implemented in the FE model and the computed overall stiffness was compared to the experimental stiffness. We found excellent agreement between experiment and modelling, as shown in Fig. 3a, demonstrating that the deformation mechanisms observed in the FE method properly describe the key mechanical response of the STinT material. The simulations and experiments show a pronounced increase in modulus (by a factor of 2.4) (Fig. 3a) with increasing spacing between the inner and outer tube, which is controlled by the Ni-layer thickness (controlled by the plating time, see Supplementary Fig. 7 and structural parameters listed in Supplementary Table 4). The 2.4-fold increase is remarkable given the fact that the densities for the 5 and 30-min plating times are almost the same (Fig. 3a). To further explore the origin of this large increase in stiffness at almost constant density, we systematically varied the stiffness, k, of the nano-struts that connect the inner tubes to the outer tubes (Fig. 3b). For very small k the inner and outer layers are effectively disconnected so that the load is only carried by the outer tube, while for very large k the inner and outer tubes are fully connected. This coupling creates a cylindrical sandwich panel with very high bending stiffness that effectively carries the external load and drastically increases the overall stiffness by one to two orders of magnitude. In summary, the FE analysis confirms that the presence of stiff nano-struts is critical to efficiently couple the inner and outer tubes, which is necessary to capture the experimentally observed 2.4-fold increase in stiffness with plating time.

Figure 3c shows FE predictions of how the mass distribution between the inner and outer tube affects the relative Young's modulus of an FCT STinT carbon structure with a relative density of $\rho/\rho_0 = 0.01$ (14 mg cm^{-3} assuming a STinT carbon wall density of 1.4 g cm^{-3}) as a function of the spacing between the inner and outer tube (experimentally controlled through the Ni-coating thickness). In general, the modulus increases from left to right with increasing Ni-layer thickness (increasing outer tube diameter). Experimental data points (black crosses in Fig. 3c, corresponding to the filled symbols in Fig. 3a) for the relative Young's modulus as a function of the (estimated) carbon mass distribution and Ni-layer thickness are superimposed on the FE predictions. Interestingly, the experimentally realized STinT morphology closely follows the ideal (highest modulus) mass distribution–inner/outer tube spacing trajectory predicted by the FE analysis, revealing that carbon dissolution and precipitation generate an optimized tube-in-tube structure. Thus, from the combination of experiment and computational modelling, the following mechanistic picture emerges, which explains the slower-than-expected decrease of stiffness of STinT carbon with decreasing density. Decreasing the density of STinT carbon requires the use of lower density polymer templates with larger log-pile pitches (and thus longer struts), which increases the Ni-layer thickness (under otherwise identical plating conditions) due to improved mass transport. This increases the stiffness of the STinT carbon structure by increasing both the contact area at the tube joints and the moment of inertia due to the larger diameter and thicker wall of the outer tube. In short, the experimentally observed modulus–density relationship, which follows a power law with an exponent of approximately 0.5 (Fig. 2), can be primarily attributed to the inverse coupling between the polymer template density (controlled by the pitch) and the Ni-coating thickness.

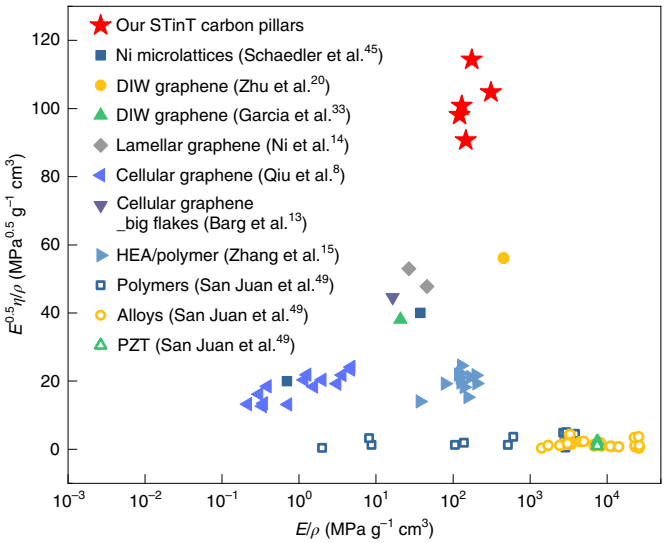

Fig. 5 | Specific damping merit index ($E^{0.5}\eta/\rho$) versus specific modulus (E/ρ). The data points for Ni microlattices, high entropy alloy (HEA)/polymer nanolattices and porous graphene materials from the literature correspond to the first cycle only. The data for our STinT pillars correspond to Fig. 4. Literature data can be found in refs. [8,13,14,19,20,45,49,50]. PZT, lead zirconate titanate.

Furthermore, cylinder-punch indentation hardness tests (as a measure of strength) revealed that the strength also decreases more slowly than expected with decreasing density. Specifically, the hardness decreases only by a factor of ~4, from 900 kPa to 200 kPa, as the density decreases by a factor of 16, from 100 mg cm^{-3} to 6.4 mg cm^{-3} (Supplementary Fig. 8).

Complementary in situ SEM micropillar compression tests provide additional insight into the local deformation mechanism (Fig. 4). These experiments show a faster decrease of the modulus with density, from 10 MPa to 2 MPa, as the density decreases from 30 mg cm^{-3} to 8 mg cm^{-3} (Fig. 2a), but this is still slower than that observed for the polymeric templates. It is important to note that we can rule out this different behaviour being an artefact of the test

geometry or procedure since we validated both test geometries (disc versus pillar) on the polymeric templates. We therefore believe that the differences in stiffness of the micropillar STinT carbon samples reflect subtle differences between nominally identical pillar and bulk materials (Supplementary Discussions).

SEM images from a 5-µm pitch STinT carbon bulk sample (Fig. 4a–c), and the corresponding engineering stress–strain curve (Fig. 4d), reveal a high degree of recovery (61% after ~26% total strain). The recovery is much higher than that observed in the corresponding cylinder-punch experiments (Supplementary Fig. 9), which we attribute to the reduced stress concentration near the edges of the angled punch compared to the cylinder punch, which can cause brittle fracture. Corresponding in situ SEM compression tests from 10-µm pitch (8.4 mg cm^{-3}) STinT carbon pillar samples with various aspect ratios, ranging from 1:1 to 2.5:1 (Fig. 4), reveal that the macroscopic deformation mode also strongly depends on confinement and the aspect ratio of the test specimen. The lateral confinement provided through the top and bottom surfaces (and the surrounding material in the case of bulk material flat-punch indentation tests) suppresses overall sample buckling and localized folding and limits shape recovery in lower aspect ratio test geometries (<2). As a result, affine compression with ~60% shape recovery after ~25% strain is observed for low (≤2) aspect ratios (Supplementary Videos 4–6), while macroscopic Euler elastic buckling with 100% shape recovery even after 50% compressive strain is observed for the high (2.5:1) aspect ratio sample (Supplementary Videos 7–9). The generally high shape recoverability is attributed to the high degree of elastic deformability of the tube-in-tube ligament morphology, high beam connectivity and low relative density. Similar recoverability has also been demonstrated in other low-density cellular materials[1,29,45,47]. To quantify the energy dissipation, we calculated the specific damping merit index shown in Fig. 5 (for more details see Supplementary Information and Supplementary Fig. 10). The low-density 2.5:1 STinT carbon pillar showed a 100% improvement of the specific damping merit index ($E^{0.5}\eta/\rho$) compared to other reported porous materials, which is attributed to the high modulus combined with pseudo-elastic buckling in the STinT carbon pillars.

The sudden drop of load at ~3.5% strain observed for the 2.5:1 ratio pillar (Fig. 4p) during the first compression cycle to 10% strain corresponds to the onset of sideways buckling originating from the bottom ~1/3 portion of the pillar (Fig. 4n). Sideways buckling, and the peak in the stress–strain curve associated with it, is not observed for more confined sample geometries, such as the smaller 2:1 (Fig. 4l) and 1:1 (Fig. 4h) aspect ratio pillars and the bulk sample (Fig. 4d). Instead, the lower aspect ratio samples show strain hardening, which becomes more pronounced with increasing confinement. The 2:1 pillar shows a transitional behaviour without the buckling-related load drop, but a much softer response (30 kPa at 20% strain) than the 1:1 pillar (60 kPa at 20% strain).

The simulations shown in Fig. 3 (and the corresponding discussion) reveal that small-strain deformation at the beam level is dominated by local symmetric bending of the elliptical tube surfaces near the scaffold joints (Fig. 3e) and longitudinal bending of the connecting tubes (Fig. 3d). For higher strain values, compression simulations reveal an additional deformation mechanism due to buckling. At the onset of elastoplastic deformation, the local symmetric bending (Fig. 3e) transitions to buckling-induced tilting (Fig. 3f,g). By accounting for a variation of the carbon tube thicknesses over the sample (using a normal distribution of the carbon thickness of the inner and outer tubes), sequential elastoplastic buckling events occur during loading (Supplementary Fig. 11), resulting in a strain-hardening response in close correspondence to the experimental stress–strain curves of the small aspect ratio samples depicted in Fig. 4d,h. The local buckling may also play a role in triggering macroscopic Euler buckling in the large aspect ratio samples (Fig. 4p) due to non-zero lateral displacements, which may occur if the tube-in-tube tilting mostly occurs in the same direction for adjacent layers (Fig. 3g).

To summarize, by developing a two-step templating approach, we were able to convert solid beams of 3D-printed polymer microlattices into hollow tube-in-tube sandwich carbon structures that resemble the morphology of animal skulls and grass stems. As a consequence of the observed coupling between the density (controlled by the pitch) of the polymeric log-pile template and spacing between the inner and the outer tubes of the STinT carbon structure (controlled by the Ni-coating thickness), the decrease in Young's modulus with decreasing density was dramatically slowed down. The STinT carbon structure also provides excellent deformation recoverability at large strains and superior specific damping properties. While the samples prepared for mechanical characterizations were in the micrometre to millimetre range, further scaling up is possible by using recently developed femtosecond projection-two photon lithography (FP-TPL) techniques[48]. More generally, developing fabrication methods that purposely break geometrical self-similarity while changing the density can be used to slow down the deterioration of modulus and strength of low-density materials with decreasing density. We hope that our results inspire novel approaches to accelerate the discovery of new advanced structural designs for low-density materials based on the optimization of local structural elements, in addition to architecture optimization.

Online content

Any methods, additional references, Nature Research reporting summaries, source data, extended data, supplementary information, acknowledgements, peer review information; details of author contributions and competing interests; and statements of data and code availability are available at https://doi.org/10.1038/s41563-021-01125-w.

Received: 25 March 2020; Accepted: 8 September 2021;
Published online: 25 October 2021

References

1. Meza, L. R., Das, S. & Greer, J. R. Strong, lightweight, and recoverable three-dimensional ceramic nanolattices. *Science* **345**, 1322–1326 (2014).
2. Bauer, J., Schroer, A., Schwaiger, R. & Kraft, O. Approaching theoretical strength in glassy carbon nanolattices. *Nat. Mater.* **15**, 438–443 (2016).
3. Biener, J. et al. Advanced carbon aerogels for energy applications. *Energy Environ. Sci.* **4**, 656–667 (2011).
4. Yang, Z.-Y. et al. Sponge-templated preparation of high surface area graphene with ultrahigh capacitive deionization performance. *Adv. Funct. Mater.* **24**, 3917–3925 (2014).
5. Oakdale, J. S. et al. Direct laser writing of low-density interdigitated foams for plasma drive shaping. *Adv. Funct. Mater.* **27**, 1702425 (2017).
6. Frenzel, T., Findeisen, C., Kadic, M., Gumbsch, P. & Wegener, M. Tailored buckling microlattices as reusable light-weight shock absorbers. *Adv. Mater.* **28**, 5865–5870 (2016).
7. Nishide, H. & Oyaizu, K. Materials science. Toward flexible batteries. *Science* **319**, 737–738 (2008).
8. Qiu, L., Liu, J. Z., Chang, S. L. Y., Wu, Y. & Li, D. Biomimetic superelastic graphene-based cellular monoliths. *Nat. Commun.* **3**, 1241 (2012).
9. Gross, J. & Fricke, J. Scaling of elastic properties in highly porous nanostructured aerogels. *Nanostruct. Mater.* **6**, 905–908 (1995).
10. Pekala, R. W., Alviso, C. T. & Lemay, J. D. Organic aerogels: microstructural dependence of mechanical-properties in compression. *J. Non Cryst. Solids* **125**, 67–75 (1990).
11. Bock, V., Emmerling, A. & Fricke, J. Influence of monomer and catalyst concentration on RF and carbon aerogel structure. *J. Non Cryst. Solids* **225**, 69–73 (1998).
12. Worsley, M. A., Kucheyev, S. O., Satcher, J. H., Hamza, A. V. & Baumann, T. F. Mechanically robust and electrically conductive carbon nanotube foams. *Appl. Phys. Lett.* **94**, 073115 (2009).
13. Barg, S. et al. Mesoscale assembly of chemically modified graphene into complex cellular networks. *Nat. Commun.* **5**, 5328 (2014).
14. Ni, N. et al. Understanding mechanical response of elastomeric graphene networks. *Sci. Rep.* **5**, 13712 (2015).

15. Zhang, X. et al. Mechanically strong and highly conductive graphene aerogel and its use as electrodes for electrochemical power sources. *J. Mater. Chem.* **21**, 6494–6497 (2011).
16. Saane, S. S. R. & Onck, P. R. Atomistic modeling of the stiffness, strength and charge-induced actuation of graphene nanofoams. *Extrem. Mech. Lett.* **5**, 54–61 (2015).
17. Qin, Z., Jung, G. S., Kang, M. J. & Buehler, M. J. The mechanics and design of a lightweight three-dimensional graphene assembly. *Sci. Adv.* **3**, e1601536 (2017).
18. Zheng, X. Y. et al. Ultralight, ultrastiff mechanical metamaterials. *Science* **344**, 1373–1377 (2014).
19. García-Tuñon, E. et al. Printing in three dimensions with graphene. *Adv. Mater.* **27**, 1688–1693 (2015).
20. Zhu, C. et al. Highly compressible 3D periodic graphene aerogel microlattices. *Nat. Commun.* **6**, 6962 (2015).
21. Bückmann, T., Thiel, M., Kadic, M., Schittny, R. & Wegener, M. An elasto-mechanical unfeelability cloak made of pentamode metamaterials. *Nat. Commun.* **5**, 4130 (2014).
22. Frenzel, T., Kadic, M. & Wegener, M. Three-dimensional mechanical metamaterials with a twist. *Science* **358**, 1072–1074 (2017).
23. Tancogne-Dejean, T., Diamantopoulou, M., Gorji, M. B., Bonatti, C. & Mohr, D. 3D plate-lattices: an emerging class of low-density metamaterial exhibiting optimal isotropic stiffness. *Adv. Mater.* **30**, 1803334 (2018).
24. Guell Izard, A., Bauer, J., Crook, C., Turlo, V. & Valdevit, L. Ultrahigh energy absorption multifunctional spinodal nanoarchitectures. *Small* **15**, 1903834 (2019).
25. Crook, C. et al. Plate-nanolattices at the theoretical limit of stiffness and strength. *Nat. Commun.* **11**, 1579 (2020).
26. Jacobsen, A. J., Mahoney, S., Carter, W. B. & Nutt, S. Vitreous carbon micro-lattice structures. *Carbon* **49**, 1025–1032 (2011).
27. Zhang, X., Vyatskikh, A., Gao, H., Greer, J. R. & Li, X. Lightweight, flaw-tolerant, and ultrastrong nanoarchitected carbon. *Proc. Natl Acad. Sci. USA* **116**, 6665–6672 (2019).
28. Meza, L. R. et al. Resilient 3D hierarchical architected metamaterials. *Proc. Natl Acad. Sci. USA* **112**, 11502–11507 (2015).
29. Zheng, X. et al. Multiscale metallic metamaterials. *Nat. Mater.* **15**, 1100–1107 (2016).
30. Oakdale, J. S., Ye, J., Smith, W. L. & Biener, J. Post-print UV curing method for improving the mechanical properties of prototypes derived from two-photon lithography. *Opt. Express* **24**, 27077–27086 (2016).
31. Xiao, X. et al. Lithographically defined three-dimensional graphene structures. *ACS Nano* **6**, 3573–3579 (2012).
32. Cebo, T. et al. Chemical vapour deposition of freestanding sub-60 nm graphene gyroids. *Appl. Phys. Lett.* **111**, 253103 (2017).
33. Garcia, A. E. et al. Scalable synthesis of gyroid-inspired freestanding three-dimensional graphene architectures. *Nanoscale Adv.* **1**, 3870–3882 (2019).
34. Gray, H. *Anatomy of the Human Body* Vol. 8 (Lea & Febiger, 1878).
35. Gibson, L. J., Ashby, M. F. & Harley, B. A. *Cellular Materials in Nature and Medicine* (Cambridge Univ. Press, 2010).
36. Karam, G. & Gibson, L. Elastic buckling of cylindrical shells with elastic cores–I. Analysis. *Int. J. Solids Struct.* **32**, 1259–1284 (1995).
37. Dawson, M. A. & Gibson, L. J. Optimization of cylindrical shells with compliant cores. *Int. J. Solids Struct.* **44**, 1145–1160 (2007).
38. Allen, H. G. *Analysis and Design of Structural Sandwich Panels* (Elsevier, 2013).
39. Sullivan, T. N., Wang, B., Espinosa, H. D. & Meyers, M. A. Extreme lightweight structures: avian feathers and bones. *Mater. Today* **20**, 377–391 (2017).
40. Xiong, W. et al. Laser-directed assembly of aligned carbon nanotubes in three dimensions for multifunctional device fabrication. *Adv. Mater.* **28**, 2002–2009 (2016).
41. Mu, X. et al. Porous polymeric materials by 3D printing of photocurable resin. *Mater. Horiz.* **4**, 442–449 (2017).
42. do Rosário, J. J., Häntsch, Y., Schneider, G. A. & Lilleodden, E. T. A combined compression and indentation study of mechanical metamaterials based on inverse opal coatings. *Acta Mater.* **195**, 98–108 (2020).
43. Ashby, M. F. The properties of foams and lattices. *Phil. Trans. R. Soc. A* **364**, 15–30 (2006).
44. Juodkazis, S., Mizeikis, V., Seet, K. K., Misawaa, H. & Wegst, U. G. K. Mechanical properties and tuning of three-dimensional polymeric photonic crystals. *Appl. Phys. Lett.* **91**, 241904 (2007).
45. Schaedler, T. A. et al. Ultralight metallic microlattices. *Science* **334**, 962–965 (2011).
46. Hashin, Z. & Shtrikman, S. A variational approach to the theory of the elastic behaviour of multiphase materials. *J. Mech. Phys. Solids* **11**, 127–140 (1963).
47. Maloney, K. J. et al. Microlattices as architected thin films: analysis of mechanical properties and high strain elastic recovery. *APL Mater.* **1**, 022106 (2013).
48. Saha, S. K. et al. Scalable submicrometer additive manufacturing. *Science* **366**, 105–109 (2019).
49. San Juan, J., No, M. L. & Schuh, C. A. Nanoscale shape-memory alloys for ultrahigh mechanical damping. *Nat. Nanotechnol.* **4**, 415–419 (2009).
50. Zhang, X. et al. Three-dimensional high-entropy alloy–polymer composite nanolattices that overcome the strength–recoverability trade-off. *Nano Lett.* **18**, 4247–4256 (2018).

Methods

Template fabrication. Log-pile lattice templates were fabricated with DLW-TPP using a commercial Nanoscribe Photonic Professional GT laser lithography system. Experimental details were identical to those described by Oakdale et al.[30] Briefly, structures were written using a Zeiss plan-apochromat ×63 1.4 NA Oil DIC M27 objective with laser peak intensities between 2 and 4 TW cm^{-2}. Macroscale DLW-TPP templates (1–2 mm in diameter, 100 µm thick) were prepared by stitching together 100 × 100 × 16 µm^3 parallelepiped log-pile blocks via repetitive galvanometer scanning of each block at a rate of 10 mm s^{-1} followed by motorized stage translations at a linear velocity rate of 40 µm s^{-1}. All of the structures were fabricated using commercial IP-Dip photoresist (lot no. 1-600-0079) obtained from Nanoscribe. The DLW-TPP templates were printed on an indium tin oxide (ITO)-coated glass slide and developed in a bath of propylene glycol monomethyl ether acetate for a period of 1 h to remove excessive resist. The ITO slide was then placed in isopropanol and UV-cured with Irgacure 651 (ref. [30]). To release the DLW-TPP templates from the glass substrate, the ITO coating was dissolved using 1 M HCl and Zn powder. Finally, the templates were placed in acetone and supercritically dried using an EMS 3100 dryer.

Microstructural characterization. A FEI 80-300 Titan transmission electron microscope was operated at 300 keV for bright-field imaging as well as high-angle annular dark-field imaging in scanning mode (HAADF-STEM) with a camera length below 130 mm to obtain *Z*-contrast pictures to reveal differences in local chemical compositions. TEM samples were prepared by gently separating tubes from each other with a sharp tweezer and placing them on a 200-mesh copper grid containing holey carbon films obtained from Ted Pella. Electron tomography was performed by collecting images from a minimum tilt range of ±70° at intervals of 3°. Images were aligned manually using IMOD (open-source program from University of Colorado, Boulder) and reconstructed using 30 iterations of the simultaneous iterative reconstruction technique using Inspect3D (FEI). Volumes were visualized in Avizo v.9.4 (FEI) by globally thresholding, performing an erosion step and then rendered using a volume render.

A Mettler XPSU Ultra microbalance (XPR2U) with readability of 0.1 µg and repeatability of 0.15 µg was used for weight measurements. A weighing paper >0.3 mg was used to hold the ultra-light samples. The measurement was repeated three more times to obtain average weight values. The relative error was typically within 8%. Thermogravimetric analysis (TGA) was carried out using a Mettler Toledo TGA/DSC 3+ (SF/1100). Nanoscribe samples with an octet-truss architecture (short diameter of 1 µm, unit cell size of 25 µm, overall sample size ≥1 mm^3) with and without Ni plating (10 min at 100 °C) were analysed. The sample was placed in a Pt crucible with a lid and heated up to 600 °C using a ramping rate of 3 °C min^{-1} under 4% H_2/N_2 atmosphere. A blank with an empty crucible was run before each experiment as a background correction.

SEM images were obtained with a JEOL7401-F SEM operated at 2–10 keV. EDS was collected under an 8-keV accelerating voltage and 10 mm working distance.

The elemental composition and areal density of films were characterized by Rutherford backscattering spectrometry (RBS) with a 2 MeV $^4He^+$ beam. The hydrogen content in selected samples was also studied by ERDA with 3 MeV $^4He^+$ ions. For RBS, the He-ion beam was incident normal to the sample surface and backscattered into a detector located at 165° from the incident beam direction. For ERDA, the sample normal direction was tilted to 70° with respect to the incident beam direction, and hydrogen atoms recoiled at 150° were measured with a surface barrier detector covered with a 10-µm-thick carbon foil. Analysis of RBS and ERDA spectra was done with the RUMP code[51]. For a further in-depth description of RBS, the reader is referred to ref. [52].

A Nicolet Almega XR dispersive micro-Raman spectrometer (Thermo Scientific) was used to analyse the nature of the STinT carbon. Spectra were collected at a wavelength, λ, of 633 nm with a ×50 objective, averaging over 25 five-second scans. Peak fitting was conducted according to refs. [53–56]. The data in the wavenumber range from 800 cm^{-1} to 2,000 cm^{-1} were deconvoluted using two Lorentzian functions (D1 band around 1,330 cm^{-1}, G band around 1,600 cm^{-1}) and two Gaussian functions (I band around 1,200 cm^{-1}, D2 band around 1,500 cm^{-1}). The G band corresponds to the in-plane stretching mode (E_{2g}) of graphite crystallites, and the D1 band corresponds to the breathing mode (A_{1g}) of the graphite crystallites related to the disorder/defect level. Detailed analysis can be found in Supplementary Fig. 14 and Supplementary Table 5.

Mechanical testing. In earlier studies[30], we measured the Young's modulus of as-printed log-pile DLW-TPP structures through micropillar compression experiments. However, in this work, the preparation of similar-sized micropillar STinT carbon structures for compression tests was not trivial, as they could not be easily tracked during the fabrication steps. Instead, most tests were performed using the flat-punch indentation method on millimetre-sized disc-shaped samples. Disc-shaped samples (~1 mm in diameter and 100 µm in thickness) were mounted on the sample stage using a thin layer of Crystalbond 509. The flatness of the discs was confirmed from side views using an optical microscope (Supplementary Fig. 1). The modulus was measured using flat-punch indentation experiments conducted on an MTS Nanoindentation XP system equipped with a 50-µm-diameter stainless steel flat-punch tip. The displacement rate was set at 1.6 µm s^{-1}. The stiffness (S) during initial unloading was measured at an indentation depth of ~10 µm to reduce densification effects. The reduced modulus, E_r, was calculated using the equation[57]:

$$E_r = \frac{\sqrt{\pi}}{2\sqrt{A}} S \quad (1)$$

where A is the area of the flat-punch indenter. The reduced modulus was defined as:

$$\frac{1}{E_r} = \frac{(1-\nu^2)}{E} + \frac{(1-\nu_i^2)}{E_i} \quad (2)$$

where E and E_i are the Young's modulus of the sample and the indenter tip (1,150 GPa), respectively. ν and ν_i are the Poisson's ratio of the sample and the indenter tip (0.07). Samples were assumed to have a Poisson's ratio of 0.2 (ref. [58]). The measured modulus represents an average response across the thickness of the sample because of the 1:2 ratio of tip diameter to sample thickness.

Multicycle cylinder-punch indentation tests were performed to check for indentation depth effects (Supplementary Fig. 9). For shallow indentations (≤10 µm, below 10% of the sample thickness of 100 µm) the effective Young's modulus increases only slowly with increasing indentation depth (Supplementary Fig. 16), thus ruling out that the higher-than-expected Young's modulus of the ultra-low-density STinT carbon discs is caused by indentation depth effects.

In situ SEM pillar compression. We did not test free-standing STinT carbon specimens, as the pillars detach from the substrate during Ni electroless plating steps, making tracking and handling of individual ~100-µm samples with a density of 10 mg cm^{-3} impractical. Instead, to perform tests on free-standing STinT carbon pillars, we integrated pillars into macroscopic plates. An array of pillars with varying densities was printed on a square plate with base plane thickness of 8 µm. After printing, the pillar showed a geometry of ~50 µm × 50 µm × 125 µm (height). The printed polymer templates were coated by electroless Ni plating following the procedures described before. To obtain complete coatings, the pillar went through the plating process twice, which was necessary to overcome the edge effects. After pyrolysis at 600 °C for 1 h and Ni removal, the STinT carbon micropillar arrays, as shown in Supplementary Fig. 17, were obtained after supercritical drying. The pillar array was placed on a silicon wafer with a thin layer Crystalbond coating and heated up to about 100 °C. The melted Crystalbond wetted the base plane and formed a rigid contact between the pillar array and the silicon substrate. The compliance from the substrate was minimized and further subtracted from in situ SEM measurements.

In situ SEM compression tests were conducted using a Bruker Hysitron PI 88 SEM PicoIndenter equipped with an extended range transducer. The instrument had a maximum displacement of 150 µm, a maximum force of 10 mN, a 1-nm displacement noise floor and a 400-nN force noise floor. A 100-µm diameter flat-ended conical conductive diamond probe was used. The indenter was placed in the chamber of a FEI Versa 3D SEM/FIB dual-beam system, allowing simultaneous recording of the mechanical response and deformation video by the PI 88 system. Compression started from out of contact but very near to the pillar surface to avoid predeformation. The strain rate for 10%, 30% and 50% deformations was set as ~10^{-3} s^{-1} using the displacement-control feedback mode of the system. The frequency for 500 cycles of 20% compression was set at 0.5 Hz.

Finite element analysis. A finite element framework was developed to simulate the STinT carbon structure. Both inner and outer carbon surfaces were constructed and discretized using shell elements in Abaqus/Standard[59]. Pitch sizes, tube diameters and thicknesses of the outer and inner carbon tubes were the input parameters. Three different staggering patterns, FCT, SC and QR, were examined. The nano-struts were incorporated as elastic springs. The struts transmit the load from the outer carbon tube to the inner tube, with the transmission efficiency being dependent on the number and stiffness of the nano-struts.

The struts were placed between every matching pair of nodes on the inner and outer tubes, such that the simulated struts connect the tubes uniformly, mimicking the observed connections in the samples (Supplementary Video 1). To do so, the discretization of the inner and outer tubes were carefully mapped against each other, resulting in 32 node pairs on each tube-in-tube cross-section, as shown in Fig. 3d. This number of pairs was chosen to balance calculation accuracy and computational costs. The 3D number density of the struts (no. of struts per µm^3) can be directly calculated from the parameters given in Supplementary Table 4 and was estimated to be around 250 struts per µm^3 by using an average inner short radius of 0.175 µm, an inner long radius of 0.6 µm; an outer short radius of 0.5 µm, an outer long radius of 1.0 µm, a spacing of the struts of 0.15 µm on the outer tube cross-section; a spacing of the struts of 0.08 µm on the inner tube cross-section and a spacing of around 0.1 µm in the longitudinal direction. The density and stiffness of the struts together determine the extent of the connectivity between the inner and outer tubes. Here, we fixed the number of struts to maximize the geometrical uniformity of their distribution and vary the strut stiffness to probe the effect of connectivity, as shown in Fig. 3b and Supplementary Fig. 18.

Carbon was modelled as a linearly elastic material, with calibrated property constants $E_0 = 32$ GPa and $\rho_0 = 1.4\,g\,cm^{-3}$ representing the Young's modulus and density of the pyrolysis-converted carbon in the fully dense state, respectively, both falling approximately within the reported ranges[60]. A typical Poisson's ratio μ_0 of 0.2 was used for the carbon[58]. Only a very small influence on the overall stiffness was found (from 0.6% to 2.5%) if the Poisson's ratio was varied from 0.2 to 0.35 (Supplementary Fig. 19).

The tube diameters and thickness values in Supplementary Table 4 were used to model the carbon pile structures (Fig. 3d). A large model with a minimum of 32 repeated unit cells was used in the z direction to overcome the edge effect from the top and bottom boundaries[61]. Periodic boundary conditions were employed along the x and y axes to mimic infinite in-plane dimensions. The bottom of the sample was assumed to be fixed in accordance with the use of Crystalbond 509 to fix the samples (see the section 'In situ SEM pillar compression'). The top of the sample was prescribed to have a uniform displacement downwards, while keeping the lateral degrees of freedom at the top unconstrained. The vertical reaction forces at the prescribed displacements were used to calculate the Young's modulus.

Data availability

The authors declare that the data supporting the findings of this study are available within the paper and its supplementary information files. Source data are provided with this paper.

References

51. Doolittle, L. R. Algorithms for the rapid simulation of Rutherford backscattering spectra. *Nucl. Instrum. Methods B* **9**, 344–351 (1985).
52. Chu, W., Mayer, J. & Nicolet, M. *Backscattering Spectrometry* (Academic Press, 1978).
53. Lespade, P., Marchand, A., Couzi, M. & Cruege, F. Caracterisation de materiaux carbones par microspectrometrie Raman. *Carbon* **22**, 375–385 (1984).
54. Vallerot, J.-M., Bourrat, X., Mouchon, A. & Chollon, G. Quantitative structural and textural assessment of laminar pyrocarbons through Raman spectroscopy, electron diffraction and few other techniques. *Carbon* **44**, 1833–1844 (2006).
55. McEvoy, N. et al. Synthesis and analysis of thin conducting pyrolytic carbon films. *Carbon* **50**, 1216–1226 (2012).
56. Schuepfer, D. B. et al. Assessing the structural properties of graphitic and non-graphitic carbons by Raman spectroscopy. *Carbon* **161**, 359–372 (2020).
57. Oliver, W. C. & Pharr, G. M. An improved technique for determining hardness and elastic-modulus using load and displacement sensing indentation experiments. *J. Mater. Res.* **7**, 1564–1583 (1992).
58. Blakslee, O., Proctor, D., Seldin, E., Spence, G. & Weng, T. Elastic constants of compression-annealed pyrolytic graphite. *J. Appl. Phys.* **41**, 3373–3382 (1970).
59. *ABAQUS/Standard User's Manual* Vol. 1 (Hibbitt, Karlsson & Sorensen, 2001).
60. Robertson, J. Amorphous carbon. *Adv. Phys.* **35**, 317–374 (1986).
61. Onck, P. R., Andrews, E. W. & Gibson, L. J. Size effects in ductile cellular solids. Part I: modeling. *Int. J. Mech. Sci.* **43**, 681–699 (2001).

Acknowledgements

We thank J.-B. Forien, M. A. Worsley, C. Zhu and X. Zheng for helpful discussions. The work was performed under the auspices of the US Department of Energy by LLNL under contract no. DE-AC52-07NA27344. The project was supported by the Laboratory Directed Research and Development (LDRD) programme of LLNL (15-ERD-019) (to J.B.). L.L. and P.R.O. would like to acknowledge financial support from the Dutch Polymer Institute (DPI) through project no. 775. Y.M.W. was partially supported by NSF DMR-2104933.

Author contributions

J.B., J.Y. and P.R.O. conceived and guided the research. J.O. and W.L.S. designed and printed log-pile structures. J.Y. performed Ni electroless plating and carbon conversion. M.M.B. assisted in post processing. J.Y. performed mechanical testing and characterizations. J.L., S.B. and J.Y. conducted in situ pillar compression tests. T.V. and J.D.R. conducted TEM and tomography analysis. M.R.C. ran the TGA analysis. L.B.B.A. carried out ERDA analysis. L.L., P.R.O. and J.v.H. conducted finite element analysis. J.Y., L.L., J.B. and P.R.O. drafted the manuscript. Y.M.W. suggested extra mechanical analysis and manuscript revisions. All authors commented on the drafts.

Competing interests

The authors declare no competing interests.

Additional information

Supplementary information The online version contains supplementary material available at https://doi.org/10.1038/s41563-021-01125-w.

Correspondence and requests for materials should be addressed to Jianchao Ye, Patrick R. Onck or Juergen Biener.

Peer review information *Nature Materials* thanks Xiaoyan Li and the other, anonymous, reviewer(s) for their contribution to the peer review of this work.